Optical Materials 84 (2018) 137–145

Contents lists available at ScienceDirect

Optical Materials

journal homepage: www.elsevier.com/locate/optmat

Red phosphor based on Eu^{3+}-doped $Y_2(MoO_4)_3$ incorporated with Au NPs synthesized via Pechini's method

Airton Germano Bispo-Jr[a,b], Gabriel Mamoru Marques Shinohara[a], Ana Maria Pires[a,b], Celso Xavier Cardoso[a,*]

[a] São Paulo State University (Unesp), School of Technology and Sciences, Presidente Prudente, SP, 19060-900, Brazil
[b] São Paulo State University (Unesp), Institute of Biosciences, Humanities and Exact Sciences, São José do Rio Preto, SP, 15054-000, Brazil

ARTICLE INFO

Keywords:
Europium(III)
Molybdates
Luminescence
Au nanoparticles

ABSTRACT

Structural, morphological and spectroscopic characterization of the Eu^{3+}-doped $Y_2(MoO_4)_3$ red phosphor incorporated with Au nanoparticles (Au NPs) synthesized via Pechini's method is reported in the present study. In order to evaluate the Au NPs and Eu^{3+} ions influence on the molybdate structure, the $Y_2(MoO_4)_3$, $Y_2(MoO_4)_3$:Eu^{3+}, $Y_2(MoO_4)_3$/Au and $Y_2(MoO_4)_3$:Eu^{3+}/Au samples were produced and fully investigated. All samples obtained at relatively low temperature, i.e., 650 °C, show molybdate as the unique phase with high crystallinity assisted by both Eu^{3+} ions and Au NPs. Water molecules detected in the molybdate structure probably are distorting MoO_4, YO_6 and EuO_6 polyhedra similarly to the Au NPs incorporated in the same lattice. These Au NPs are spherical-shaped with a diameter near to 46 nm and they are located on the molybdate particle surface. The Eu^{3+}-doped phosphors, with or without the presence of Au NPs, exhibit intense red luminescence characteristic of the Eu^{3+} ion inserted in low-symmetry sites. However, the Au NPs increase the radiative emission rate and absolute quantum yield of the Eu^{3+} $^5D_0$ emitter state due to the excitation field enhancement caused by the local surface plasmon resonance absorption effect of gold nanoparticles, which was confirmed by diffuse reflectance measurements. Finally, the Eu^{3+} quantum efficiency enhancement to 92% played by the gold nanoparticles and the high red color purity qualify the obtained phosphor for photonic applications.

1. Introduction

Nowadays, the combination of Au nanoparticles (Au NPs) and phosphors has attracted a lot of attention in the photonic field due to their applicability as drug delivery, diagnosis, therapeutics, and fluorescent probes in the detection of metal ions, small molecules, and biomacromolecules. [1–5] This wide field of applications comes from the synergism between the phosphor luminescence and the AuNPs properties, such as good conductivity and favorable biocompatibility [6]. Therefore, in the present study, the $Y_2(MoO_4)_3$:Eu^{3+}/Au composite is introduced aiming to combine both phosphor's and Au NPs properties which can provide bifunctionalities for high sensitivity/resolution fluorescence imaging and high quality in the detection of different molecules [7].

Eu^{3+} ion, in its turn, is a well-know red activator due to its emission lines that arise from the $^5D_0$ excited level to the $^7F_{0-6}$ ground states. [8–10] Besides the efficient emission, the Eu^{3+} ion can also act as structural probe because its main emission lines are sensitive to the crystalline field around the metal ion [11]. Usually, the Eu^{3+} ion is inserted in a host matrix such as oxides [12] or silicates [13] in order to enhance the Eu^{3+} absorptivity due to the sensitization effect played by the matrix. In this context, yttrium molybdate, $Y_2(MoO_4)_3$, is a suitable host for the Eu^{3+} ion due to its low relative phonon frequency, high thermal and electrical stability, high UV absorption of the MoO_4 groups, and the similar radii between Y^{3+} and Eu^{3+} ions. [14,15] The synthesis of $Y_2(MoO_4)_3$:Eu^{3+} phosphor via solid-state [14] or co-precipitation [16] methods are already reported in the literature; however, to date, no reference has been found on the use of the Pechini's method to obtain such material. In this way, the Pechini method was chosen in this present study for the preparation of the red phosphor $Y_2(MoO_4)_3$:Eu^{3+} based on the fact that it is a simple, and low-cost methodology, that allows good structural and stoichiometric control in the synthesis of high purity metal oxide particles. [17,18].

Metallic nanoparticles, as already mentioned, have been intensely used as active component in biosensors or drug delivery systems. [19,20] In this field, Au NPs have been highlighted because of their optical properties dependent on shape and size, and due to their quantum confinement effects [21]. For instance, due to their relative

* Corresponding author. São Paulo State University (Unesp), School of Technology and Sciences, R. Roberto Simonsen, 305, 19060-900, Presidente Prudente, SP, Brazil.
E-mail address: xavier.cardoso@unesp.br (C.X. Cardoso).

https://doi.org/10.1016/j.optmat.2018.06.023
Received 26 April 2018; Received in revised form 30 May 2018; Accepted 14 June 2018
Available online 02 July 2018

inertia and surface Plasmon absorption bands in the visible and near-infrared spectral regions, Au NPs have been used as SERS (surface-enhanced Raman scattering) substrates [22]. To the best of our knowledge, there is no report in the literature about the $Y_2(MoO_4)_3:Eu^{3+}$/Au composite synthesis. Furthermore, there is a challenge to be overcome in the synthesis of phosphors incorporated with gold nanoparticles in relation to the shape and size control of the metallic nanoparticles during the calcination step. Thus, the aim of this study is to synthesize the $Y_2(MoO_4)_3:Eu^{3+}$/Au composite applying an adapted Pechini methodology, in order to evaluate the effects of the Eu^{3+} ions and Au NPs in the structural, morphological, and luminescent properties of the produced composite.

2. Material and methods

2.1. Experimental

Rare earth oxides, (Y_2O_3 and Eu_2O_3, 99.99%, Sigma-Aldrich), ammonium molybdate tetrahydrate ($(NH_4)_6Mo_7O_{24}.4H_2O$, 99.9%, Sigma-Aldrich), gold (III) chloride trihydrate ($HAuCl_4.3H_2O$, Sigma-Aldrich), D-sorbitol ($C_6H_{14}O_6$: 99%, Sigma-Aldrich), anhydrous citric acid ($C_6H_8O_7$: 99.5%, Fluka Analytical), and nitric acid, (HNO_3, 65%, VETEC) were used as starting materials without further purification.

$Y_2(MoO_4)_3$, $Y_2(MoO_4)_3:Eu^{3+}$, $Y_2(MoO_4)_3$/Au and $Y_2(MoO_4)_3:Eu^{3+}$/Au powders were synthesized based on the modified Pechini's method reported to the preparation of $Y_2O_3:Eu^{3+}$ phosphors [23,24] however, in the present case, using sorbitol as complexing agent instead of ethyleneglycol. The percentage of 2 at% of Eu^{3+} in relation to Y^{3+} ions was chosen to provide phosphors with good and comparable light-emitting properties [25]. Therefore, rare earth nitrate solutions (prepared by dissolving stoichiometric amounts of the rare-earth oxides in HNO_3) were added in citric acid (molar ratio of citric acid to rare earth of 3:1) in order to obtain 0.5 g of the final powder. The mixture was kept upon mechanical stirring until the acid dissolution at 80 °C for 10 min, and then stoichiometric amounts of ammonium molybdate tetrahydrate were added. At this moment, the solution acquired a yellow color. After 10 min, stoichiometric amounts of sorbitol (molar ratio of sorbitol to rare earth of 2:1) was added. After 20 min, just in the case of $Y_2(MoO_4)_3$/Au and $Y_2(MoO_4)_3:Eu^{3+}$/Au samples preparation, the gold (III) chloride trihydrate (in weight percent of 2 wt% in relation to 0.5 g of the final powder) was added. The solution was heated at 120 °C under mechanical stirring for 1 h until the polymeric resin formation. The polymeric resin was submitted to a pre-calcination at 400 °C for 5 h. After this treatment, the partial decomposition of the resin took place, yielding the so-called puff (expanded resin). This material was ground in a mortar and sieved in a 325-mesh sieve. Then, the powder was heated again at 650 °C in air atmosphere for 5 h [26]. The $Y_2(MoO_4)_3:Eu^{3+}$ and the undoped matrix were also synthesized in order to evaluate the gold and europium impacts in the molybdate structure.

2.2. Characterization

Powder X-ray diffraction (XRD) was carried out in a SHIMADZU XDR-6000 diffractometer, step size of 0.02°, Cu $K\alpha_1$ radiation $\lambda = 1.5406$ Å. The crystallite size of the samples was calculated via Scherrer's method [27], equation (1).

$$\varepsilon = \frac{K\lambda}{\beta_p cos\theta} \quad (1)$$

Where βp is the width at half maximum in radians of a reflection peak; k is a constant that depends on the reflection symmetry, which usually is given as 0.9; ε is the grain size, and λ is the X-ray wavelength in nanometer.

The thermal profile of the samples was checked through thermogravimetry (TG) and differential scanning calorimetry (DSC) using a TA Instruments, model SDT Q600, and heating ramp of 10 °C/min. The thermal treatment was performed from 25 ºC to 1000 °C, under a nitrogen atmosphere (100 mL/min). The vibrational profile of the samples was monitored by Fourier transform infrared spectroscopy (FTIR) in KBr pellets by using a SHIMADZU IRAFFINITY-1 spectrophotometer and by Raman spectra obtained in a RENISHAW IN-VIA spectrometer equipped with a LEICA DMLM optical microscope. The morphology was checked by scanning electron microscopy (SEM) measurements by using a CARL ZEISSEVO LS15 microscope and by transmission electron microscopy (TEM) in a JEOL microscope, JEM-2100 model. The samples were also characterized by UV–Vis diffuse reflectance measurements in a PERKIN ELMER LAMBDA 1050 spectrophotometer in order to evaluate the band gap of the phosphors through a graphic of $(\alpha h\nu)^n$ versus the energy of the incident photon (h), where n has a value equal to 2 for direct transition and 0.5 for indirect transition [28]. The α value is the ratio of the scattering and absorption coefficients according to the Kubelka-Munk's approximation [29], equation (2), where R is the reflectance observed for the different incident energies.

$$\alpha = \frac{K}{S} = \frac{(1-R)^2}{4R} \quad (2)$$

Photoluminescence (PL) spectroscopy, at room temperature, for all produced phosphors were measured under continuous Xe lamp (450 W) excitation in a HORIBA JOBIN YVON FLUOROLOG-3 spectrofluorimeter equipped with an excitation and emission double monochromator and a photomultiplier R 928 HAMMATSU. The slits were placed at 2.0 and 0.5 nm for excitation and emission, respectively. The emission decay curves were carried out in a phosphorimeter equipped with Xe (5 J/pulse) lamp. The Judd-Ofelt intensity parameters Ω_2 and Ω_4 were estimated for all Eu^{3+} phosphors from the emission data by using equations (3) and (4) [30], where $\langle {}^5D_0 \| U^\lambda \| {}^7F_1 \rangle$ represents the square reduced matrix elements which values are equal to 0.0032 to Ω_2 and 0.0023 to Ω_4 [30]; h is the Planck's constant, e is the electron charge, c is the speed of light in vacuum, ε_0 is vacuum permittivity constants. A_{01} can be estimated by the equation $A_{01} = 14.65\ n^3$ in s^{-1} [31], where n is the refractive index, equal to 2.031 for the molybdate [32]. I is the integrated area under the ${}^5D_0 \rightarrow {}^7F_j$ transitions in the emission spectra. X is the Lorentz local field correction equal to $n(n^2+2)^2/9$.

$$A_{0-\lambda} = A_{0-j} = A_{01}\frac{I_{0-j}}{I_{0-1}}\frac{h\nu_{0-1}}{h\nu_{0-j}} \quad (3)$$

$$\sum_{\lambda=2,4} \Omega_\lambda {}^5D_0 \| U^{(\lambda)} \| {}^7F_j^2 = A_{01}\frac{I_{0-j}}{I_{0-1}}\frac{h\nu_{0-1}}{h\nu_{0-j}}\frac{3hc^3 4\varepsilon_0}{64\pi^3 e^2}\frac{1}{\nu_\lambda{}^3 x} \quad (4)$$

The emission decay curves were used to estimate the emission lifetime (τ) that were applied to evaluate the Eu^{3+} quantum efficiency (η_{Eu}). The quantum efficiency is calculated by applying equation (5), where A_{rad} and A_{nrad} are the radiative and the non-radiative rates for an emitting level, respectively.

$$\eta = \frac{A_{rad}}{A_{rad} + A_{nrad}} \quad (5)$$

The A_{rad} rate was estimated by equations (3) and (6), and the A_{nrad} from equation (7).

$$A_{rad} = \sum_J A_{0-j} \quad (6)$$

$$A_{total} = \frac{1}{\tau} = A_{rad} + A_{nrad} \quad (7)$$

Finally, the absolute emission quantum yield values (QY) were measured at room temperature by using a UV-NIR absolute PL quantum yield spectrometer C13534 from Hamamatsu under continuous Xe lamp

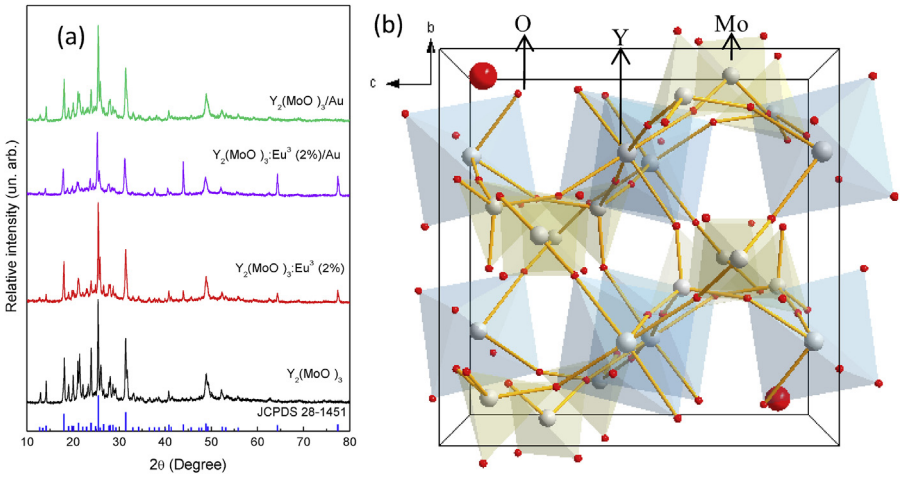

Fig. 1. Powder X-ray diffraction patterns of $Y_2(MoO_4)_3$, $Y_2(MoO_4)_3$/Au, $Y_2(MoO_4)_3$:Eu^{3+}(2%) and $Y_2(MoO_4)_3$:Eu^{3+}(2%)/Au prepared by the Pechini's method compared with JCPDS-28-1451 card (a). $Y_2(MoO_4)_3$ unit cell representation, based on the CIF file (COD-1535040) [36] available on Inorganic Crystal Structure Database (ICSD) (b). The MoO_4 polyhedra are represented in yellow, the YO_6 in blue and the oxi ions in red. (For interpretation of the references to color in this figure legend, the reader is referred to the Web version of this article.)

(150 W). The emission quantum yield is given by Equation (8), where N_{Em} and N_{Abs} are the number of photons emitted and absorbed by the sample, respectively; I_{em}^{sample} and $I_{em}^{reference}$ are the emission intensities with and without a sample, respectively, in the wavelength interval (λ_1,λ_2); and I_{ex}^{sample} and $I_{ex}^{reference}$ are the integrated intensities of the excitation radiation measured with and without a sample, respectively, in the excitation wavelength interval (λ_3,λ_4) [33].

$$QY = \frac{N_{Emi}}{N_{Abs}} = \frac{\int_{\lambda_1}^{\lambda_2} \frac{\lambda}{hc}(I_{Em}^{sample}(\lambda) - I_{Em}^{Reference}(\lambda))d\lambda}{\int_{\lambda_3}^{\lambda_4} \frac{\lambda}{hc}(I_{Ex}^{sample}(\lambda) - I_{Ex}^{Reference}(\lambda))d\lambda} \quad (8)$$

3. Results and discussion

All synthesized samples exhibit X-ray diffraction patterns, Fig. 1 (a), primarily corresponding to a monophasic material identified from the JCPDS database as belonging to orthorhombic $Y_2(MoO_4)_3$ (P_{bcn}) (JCPDS 28–1451) structure [34]. Regarding the limit of detection of this technique, no diffraction peaks characteristic for the europium, yttrium, or molybdate oxides are detected, which corroborate for the fact that Eu^{3+} ion is inserted into the $Y_2(MoO_4)_3$ lattice. The background noise observed in the XRD patterns is correlated to the molybdate hygroscopicity [35]. When Au or Eu^{3+} are present in the system, the diffraction peaks coincide exactly with the standard card, as shown in Table 1, indicating that both Eu^{3+} and Au NPs are favoring the matrix crystallization.

The orthorhombic $Y_2(MoO_4)_3$ is composed by corner-sharing YO_6 octahedra and MoO_4 tetrahedra as represented in Fig. 1 (b). Each YO_6 octahedron is connected to six MoO_4 polyhedra, and each MoO_4 polyhedron is bonded to four YO_6 octahedra [26]. Also, the polyhedra are slightly distorted, with Y–O bond distances lying between 2.17 and 2.31 Å and Mo–O bond distances between 1.66 and 1.84 Å [26]. All samples doped with Eu^{3+} or incorporated with Au have crystallite size smaller than the undoped sample, as shown in Table 1. Samples incorporated with Au exhibit crystallite size even smaller than that of the Eu^{3+}-doped ones, suggesting that Au decreases the crystallite size of $Y_2(MoO_4)_3$. Eu^{3+}-doped samples exhibit a crystallite size decrease, themselves, due to the reduction of the strain in the molybdate network caused by the doping since Eu^{3+} is smaller than Y^{3+} ions [37]. After the Au NPs incorporation, in turn, the gold particles stay on the surface of the molybdate particles inhibiting their growth, a fact that will be confirmed ahead by TEM images.

Table 1
Interplanar distance (d), intensity ratio (I/I_0), half-width (FWHM) and crystallite size (ε) for the three most intense plans of $Y_2(MoO_4)_3$ powders.

Samples	2θ (°)	d (Å)	I/I_0	FWHM	ε (nm)
$Y_2(MoO_4)_3$	18.0	4.89	0.45	0.255	46
	25.4	3.50	1	0.214	63
	31.4	2.84	0.63	0.294	41
$Y_2(MoO_4)_3$:Eu^{3+}(2%)	18.0	4.91	0.43	0.267	43
	25.4	3.49	1	0.226	58
	31.4	2.84	0.55	0.416	26
$Y_2(MoO_4)_3$/Au	18.0	4.91	0.45	0.297	38
	25.4	3.49	1	0.270	44
	31.4	2.84	0.57	0.461	23
$Y_2(MoO_4)_3$:Eu^{3+}(2%)/Au	18.0	4.91	0.45	0.305	38
	25.4	3.52	1	0.252	49
	31.4	2.86	0.61	0.441	24
JCPDS 28-1451	18.0	4.91	0.3	–	–
	25.4	3.52	1	–	–
	31.4	2.85	0.7	–	–

The TG curves of the as-prepared powder molybdates, Fig. 2 (a), show an intense weight loss at 100 °C, due to the water loss. A similar behavior, but in the range between 60 and 120 °C, was observed in some other hygroscopic phases, such as $Y_2W_3O_{12}$ [38], $Er_2W_3O_{12}$, $Yb_2W_3O_{12}$, and $Lu_2W_3O_{12}$ [39]. While the TG heating curves of $Y_2(MoO_4)_3$ with Eu^{3+} and Au have just one loss weight at 100 °C, in the $Y_2(MoO_4)_3$TG heating curve, a second loss weight at 200 °C is observed. B.A. Marinkovic et al. (2005) [40] reported a similar behavior and attributed it to the presence of two differently bonded water species in the $Y_2(MoO_4)_3$ matrix. Furthermore, from 100 °C, the sample weight increases for all samples. A similar behavior was verified in the study of B.A. Marinkovic, but this peculiar characteristic for this system is not well-known in the literature yet [40]. From TG measurements, it is possible to evaluate the water amount in each sample, which is nearly to 3 mol by 1 mol of $Y_2(MoO_4)_3$. This pattern corresponds to the trihydrate, $Y_2(MoO_4)_3.3H_2O$, which has been previously reported in the literature [40]. The DSC curves, Fig. 2 (b), show an endothermic peak at 100 °C assigned to water evaporation, in accordance with TG measurements. Displacement at the water outlet temperature for the undoped $Y_2(MoO_4)_3$ matrix can be related to the presence of two differently bonded water species.

According to the TG and DSC results, the $Y_2(MoO_4)_3$ powder is rather hygroscopic. B.A. Marinkovic et al. showed that the water molecules occupy microchannels with diameter around 5 Å along *c*-crystallographic directions in $Y_2(MoO_4)_3$ structure, leading to a negative thermal expansion in $Y_2(MoO_4)_3$ [38]. Furthermore, M. Wu et al. showed that the water absorption reduces the Y-Mo bond distance, shortening the Y-O-Mo bond angle and consequently reducing the solid volume [41].

Results achieved through FTIR and Raman spectroscopy for molybdate samples are shown in Fig. 3. FTIR spectra, Fig. 3(a), reveal a band at about 1000 - 700 cm^{-1} assigned to the symmetric stretching mode of M-O bonds and a second band at 1612 cm^{-1} assigned to O-H

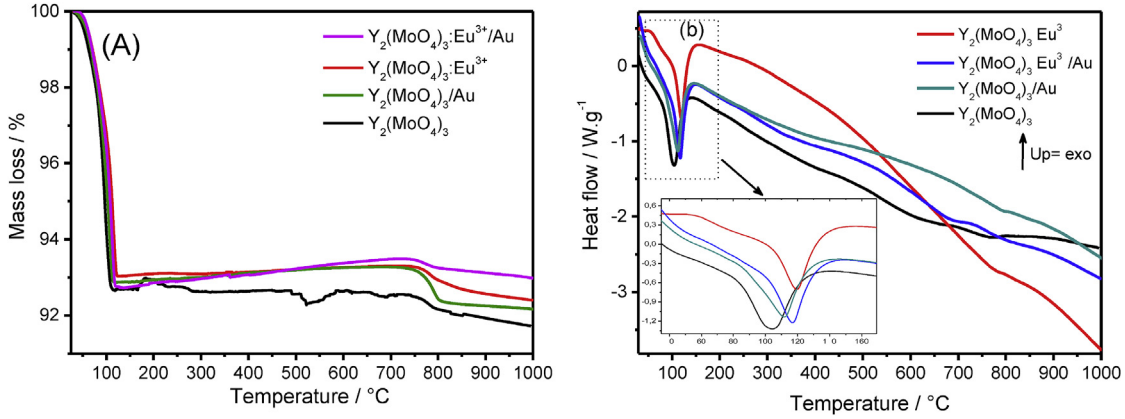

Fig. 2. Themogravimetry (TG) (a) and differential scanning calorimetry (DSC) (b) analysis for $Y_2(MoO_4)_3$, $Y_2(MoO_4)_3$/Au, $Y_2(MoO_4)_3$:Eu^{3+}(2%) and $Y_2(MoO_4)_3$:Eu^{3+}(2%)/Au powder obtained from the calcination at 650 °C.

bond in H_2O molecules. No shifts were observed for vibrational modes referring to M-O bond in FTIR spectra when the four samples are compared, indicating that gold is not inserted in the molybdate network. If gold was inserted into Y^{3+} sites in the molybdate lattice, it would be expected shifts in the vibrational modes of O-M bonds, since the ionic radius of Au and Y^{3+} are very different, leading to distortions in the matrix network and changes in the Y-O bond lengths. Already in the case of Eu^{3+} and Y^{3+}, the ionic radii are very close and such displacements are not expected, confirming that Eu^{3+} ions are replacing Y^{3+}.

In the Raman spectra, Fig. 3(b), the stretching modes of the $[MoO_4]^{2-}$tetrahedra can be found in the range of 800–980 cm^{-1}, and the deformation modes are situated between 200 and 400 cm^{-1} [42]. The three broad Raman bands around 945, 830, and 340 cm^{-1} can be identified as symmetric stretching (ν1), asymmetric stretching (ν3), and symmetric (ν2) bending phonon modes of the $[MoO_4]^{2-}$tetrahedra, respectively [43]. Also, the absence of Eu_2O_3 vibrational modes confirms that Eu^{3+} ions are inserted in the $Y_2(MoO_4)_3$ lattice. Three samples show the same spectral profile and only the Eu^{3+}-doped and incorporate with Au sample show a different spectral profile, which is directly related to $[MoO_4]^{2-}$ polyhedra symmetry changes. T. Schleid et al. demonstrated that the $[MoO_4]^{2-}$ polyhedra has *Cs* symmetry [44]. Also, according to G. Busca [42], the $[MoO_4]^{2-}$ polyhedra can have a C_1 symmetry. In this case, one symmetric stretching and three asymmetric modes can be detected in the Raman spectrum, with the symmetric mode at higher energy. For $Y_2(MoO_4)_3$:Eu (2%)/Au sample, we assume that the peak at 953 cm^{-1} in the Raman spectrum is the symmetric one, and those at 864, 813, and 795 cm^{-1} are the asymmetric modes. Also, the intensity decrease of the band at 350 cm^{-1} is due to the lowering of the MoO_4 symmetry. [42,44] In this way, when the Eu^{3+} ion and Au are present in the host, it is occurring a symmetry lowering of the $[MoO_4]^{2-}$polyhedral since the C_1 point group is less symmetric than the C_s one. Changes in the $[MoO_4]^{2-}$ polyhedra symmetry will also influence in modifications in the YO_6 and EuO_6 polyhedra.

The surface morphology of the molybdates was evaluated through SEM, Fig. 4. For all four samples, particle aggregates are observed. The blocks consist of particles with grain sizes around 1126, 879, 995 and 994 nm for $Y_2(MoO_4)_3$, $Y_2(MoO_4)_3$:Eu^{3+}(2%), $Y_2(MoO_4)_3$/Au and $Y_2(MoO_4)_3$:Eu^{3+}(2%)/Au respectively, and oriented growth is not observed. R. Krishnan et al. [45] and S. F. Wang et al. [46] found similar profiles for $(Na_{0.5}Gd_{0.5})MoO_4$:Eu^{3+} and $Y_2(MoO_4)_3$:Eu^{3+} respectively. In our case, particles with some agglomeration are characteristic of the Pechini's method, which typically yield particles with high grain size in the form of particle agglomerates. Eu^{3+}-doped or incorporated with Au samples exhibit particle size smaller than that of the undoped matrix, which is related to the crystallite size decrease verified by XRD data. The particle contours visualized by SEM images are agglomerates of nanocrystallites, thus, if the nanocrystallite size decreases when the molybdate is incorporated with Au NPs or doped with Eu^{3+}, the particle size is expected to decrease equally.

Fig. 5 shows the TEM images of $Y_2(MoO_4)_3$:Eu^{3+}(2%)/Au particles. The viewed particles are agglomerated as in the SEM images and three regions with different image contrast are observed. In each region, it was performed energy-dispersive spectroscopy (EDS) analysis, Figure S1. It can be noticed in the region A atomic planes with an interplanar spacing of 0.345 nm corresponding to the diffraction plane of the

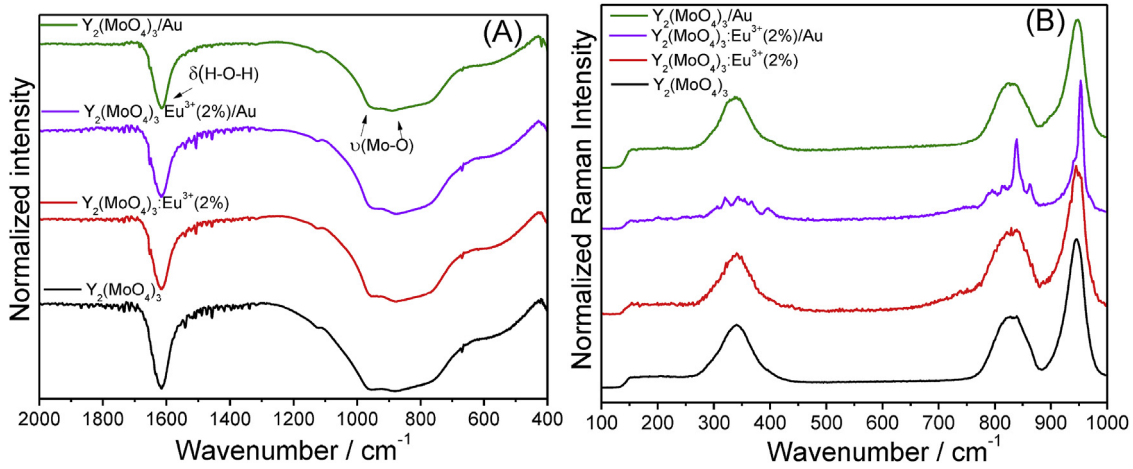

Fig. 3. FTIR (a) and Raman (b) spectra for $Y_2(MoO_4)_3$, $Y_2(MoO_4)_3$/Au, $Y_2(MoO_4)_3$:Eu^{3+}(2%) and $Y_2(MoO_4)_3$:Eu^{3+}(2%)/Au powders.

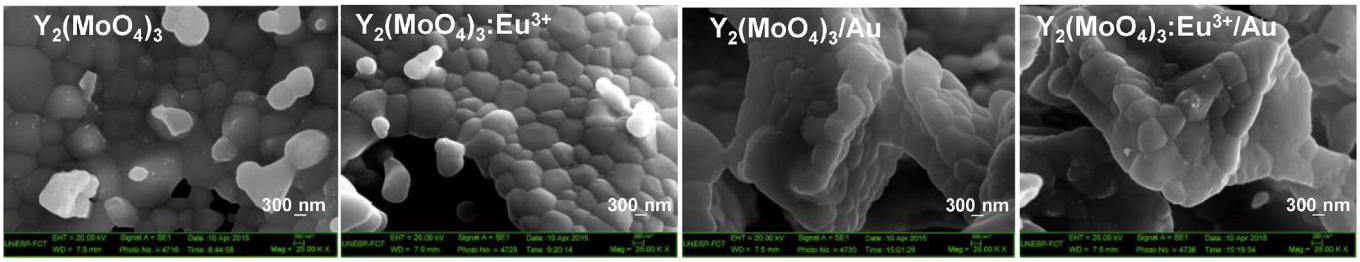

Fig. 4. SEM images for $Y_2(MoO_4)_3$, $Y_2(MoO_4)_3$:Eu^{3+}(2%), $Y_2(MoO_4)_3$/Au and $Y_2(MoO_4)_3$:Eu^{3+}(2%)/Au powders.

$Y_2(MoO_4)_3$ phase at 25.40°. The well-defined diffraction pattern image suppresses any doubt that the XRD measurements can give about the molybdate crystallinity. Through EDS measurement, the elements Y, Mo, and O are detected in the A region, indicating that the particle corresponds to $Y_2(MoO_4)_3$ with high crystallinity. In the B region, as just Au atoms are detectable through EDS, it is feasible to say that the spherical particles correspond to Au, with an average diameter near 46 nm. Besides that, the spherical particle shows interplanar spacing of 0.30 nm corresponding to the (1 1 0) plane of the cubic Au phase (JCPDS-04-0784) [47]. In the C region, Au, Y, Mo and O are observed, which probably means that this region corresponds to Au particles inside the $Y_2(MoO_4)_3$ particle or even on the particle surface, but seen by a superior angle.

Diffuse reflectance spectra of all samples were acquired in the UV–Vis region, Fig. 6. The strong absorbance at around 567 nm due to plasmon resonance of gold detectable only in the samples where Au was inserted indicates that these metal nanoparticles are effectively incorporated in the $Y_2(MoO_4)_3$ matrix [48]. The Au NPs plasmon resonance band arises from the mutual oscillation of free electrons on the Au NPs surface, creating a dipole with a resonance frequency in the visible spectra region [49]. The diffuse reflectance spectra also exhibit a strong and sharp absorption in the higher energy region with the maximum near to 225 nm related to transitions of the valence band

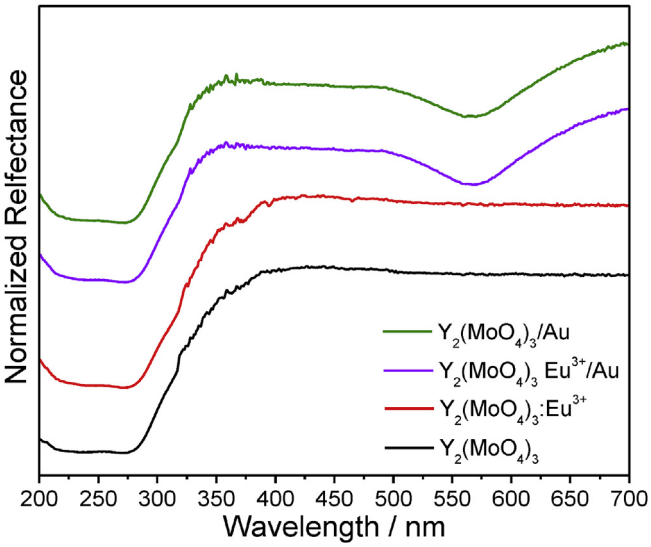

Fig. 6. Diffuse reflectance spectra of $Y_2(MoO_4)_3$, $Y_2(MoO_4)_3$/Au, $Y_2(MoO_4)_3$:Eu^{3+}(2%) and $Y_2(MoO_4)_3$:Eu^{3+}(2%)/Au.

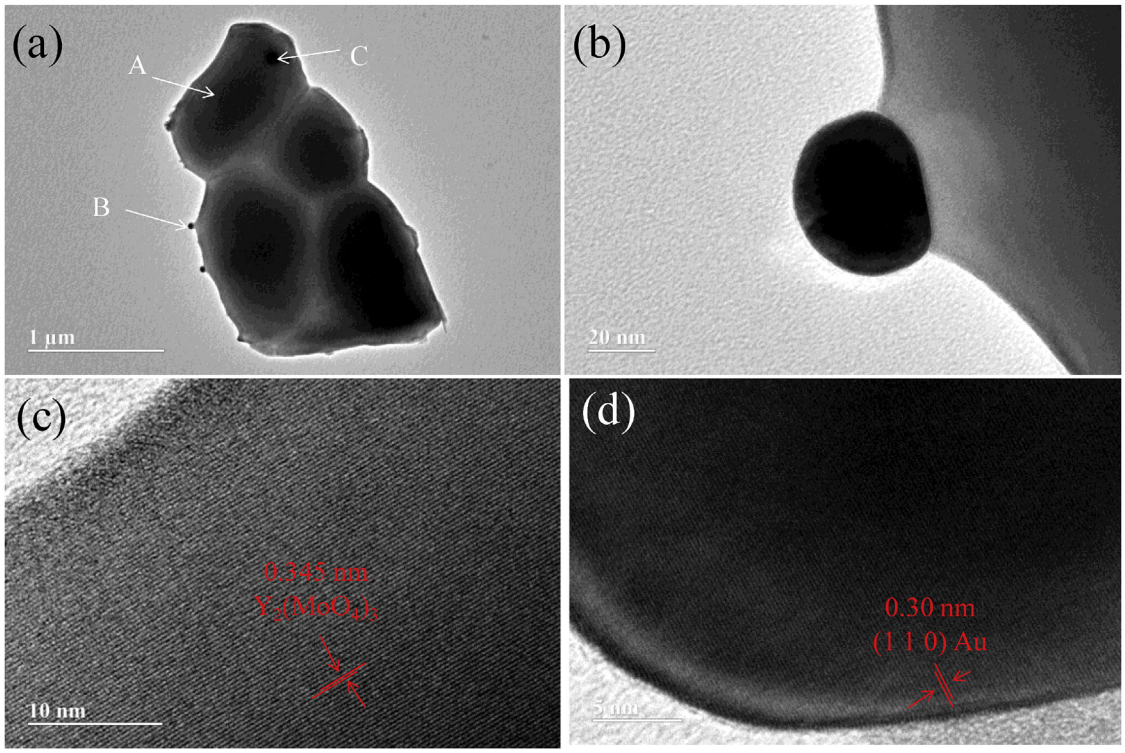

Fig. 5. TEM images of $Y_2(MoO_4)_3$:Eu^{3+}(2%)/Au composite (a) Au NP region (b), magnification in the $Y_2(MoO_4)_3$ particle (c), and magnification in the Au NP region (d).

(VB) and conduction band (CB) that correspond to the band gap of the material and to the Eu^{3+}-O^{2-} and Mo^{6+}-O^{2-} charge transfer bands. The band gap values of the molybdate powders were estimated by the Kubelka-Munk's approximation considering direct transitions as shown in Figure S2. The direct transitions are chosen due to their better adjustment than that of indirect transitions, as shown in Figure S3. In the obtained plots viewed in Figure S2, the curve extrapolation to the zero ordinate value provides the band gap energy estimative. Also, by the Kubelka-Munk's approximation, it was possible to separate the band gap transition and the charge transfer bands in the DR spectra, as shown in Figure S3. The calculated bandgap value for the undoped molybdate is 3.49 eV and it is in accordance with the value reported in the literature by R. Velchuri et al. [50] For the other samples, the band gap value decreases to 2.45 eV, 2.80 eV, and 2.90 eV when Au NPs, Eu^{3+} ions, and Au NPs/Eu^{3+} are added in the system, respectively. This band gap reduction is associated with the particle size decrease, as shown by SEM images, and to the presence of Au and Eu^{3+} energy levels that lie between the VB and CB. When the particle size decreases, the surface area enhances, increasing the surface defect concentration in the system, due to unfiled Mo, Y and/or Eu^{3+} sites. These surface defects lead to the arising of electronic levels that lie between the VB and CB, decreasing the molybdate band gap. Also, the electronic levels that come from Eu^{3+} and Au NPs will lead to changes in the band gap, justifying the band gap value changes in the doped or incorporated samples.

The undoped samples excited under 294 nm exhibit a broad band in the red region, as shown in the emission spectra at room temperature, Fig. 7. Some authors have assigned this red emission to defects on the molybdate structure surface [51–53] and to the existence of molybdate group lacking an oxygen ion [54]. This defects can be interpreted as being Frenkel like defects (oxygen ion shifted to the inter-site position with simultaneous creation of vacancy) in surface layers of the prepared $Y_2(MoO_4)_3$ particles. [52,55].

The excitation and emission spectra at room temperature of the Eu^{3+}-doped molybdate phosphors are viewed in Fig. 8. Both excitation spectra show a broad band with a maximum at about 271 nm assigned to the Eu^{3+}-O^{2-} charge transfer (CT) band and to the O^{2-}-Mo^{6+} CT band which dominates the excitation profile, Fig. 8 (a), as well as narrow and week lines related to the Laporte forbidden Eu^{3+} *f-f* transitions, which is responsible for their lower intensities. The broad intense band in the deep-UV region is a sum of the Eu^{3+}-O^{2-} CT band and the energy-transfer from molybdate groups to Eu^{3+} ions in the molybdate network. In fact, the literature shows that it is not easy to distinguish both bands in the excitation spectra [56].

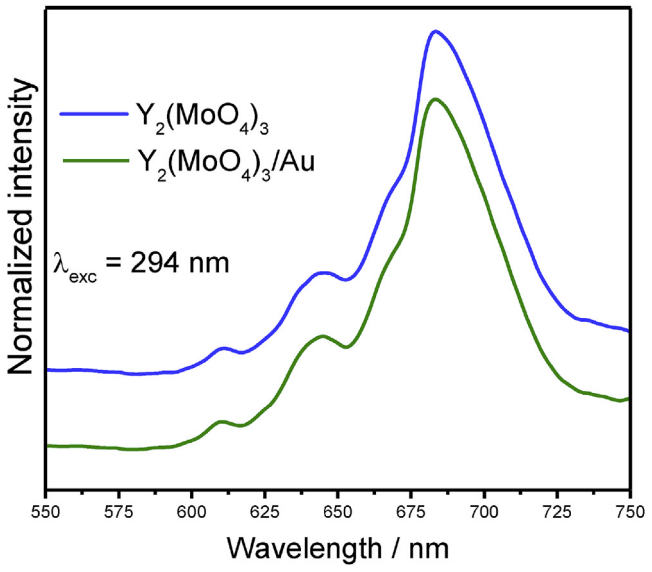

Fig. 7. Room-temperature emission spectra under 294 nm excitation of the undoped $Y_2(MoO_4)_3$ particles prepared by Pechini's method with and without Au NPs.

The corresponding emission spectra using the 270 nm excitation in the CT band shown in Fig. 9(b) displays a set of transitions from the Eu^{3+} $^5D_0$ excited level to the $^7F_{0,1,2,3,4}$ ground levels in the red region. No emission band corresponding to molybdate group is detectable which clearly suggests that the energy absorbed by the MoO_4 group is transferred to Eu^{3+} levels. The emission spectra are mainly dominated by the hypersensitive $^5D_0 \rightarrow {}^7F_2$ transition characteristic of Eu^{3+} ions in low symmetry sites. Besides that, the presence of $^5D_0 \rightarrow {}^7F_0$ transition in the emission spectra indicates that the Eu^{3+} ion is inserted in a site without inversion center since this transition, according to symmetry selection rules, is only allowed when the Eu^{3+} is occupying sites without inversion center [57]. As shown via XRD, the Eu^{3+} ions are replacing the YO_6 octahedra in the molybdate lattice; these polyhedral are distorted and as consequence, there is no inversion center in the EuO_6 polyhedra, justifying the Eu^{3+} low symmetry sites.

The Eu^{3+} $^5D_0 \rightarrow {}^7F_0$ (0-0) transition is forbidden but its selection rules are relaxed when the Eu^{3+} ion is inserted in a site without inversion center. Furthermore, just one component for each Eu^{3+} non-equivalent site is expected. In fact, only one component for the 0-0 transition can be seen in the emission spectra for both samples, confirming that Eu^{3+} is occupying just one site without inversion center. Already the Eu^{3+} 0–2 transition is a pseudo-quadrupole transition with a maximum of 5 components for each Eu^{3+} site. In this case, at least five components can be seen in the emission spectra for both samples. However, for the Au NPs-incorporated molybdate, these components are not well-defined and probably it is related to the decrease of Eu^{3+} site symmetry caused by Au NPs.

The CIE (International Commission on Illumination) chromaticity diagrams obtained for both Eu^{3+}-doped phosphors (see Figure S4, supplementary material) show 100% of red color purity at 270 nm excitation and (x; y) CIE coordinates equal to (0.67; 0.32) and (0.66; 0.33) for the Eu-doped and Eu-doped/Au molybdates, respectively.

The A_{rad} values (Table 2) calculated from the emission spectra and equation (3), and (6) are directly related to the radiative process from the Eu^{3+} $^5D_0$ emitter level to the ground levels, and they increase when the Au NPs are inserted in the system. On the other hand, the non-radiative losses decrease for the Au incorporated sample. This Eu^{3+} emission improvement played by Au NPs can be attributed to the excitation field enhancement caused by the local surface plasmon resonance absorption effect of Au nanoparticles [58]. It is well-known in the literature that noble metal NPs can enhance the Eu^{3+} luminescence and it can be explained by the radiating plasmons (RPs) model [59].In Fig. 9 it is been shown an illustration of this model in the molybdate structure [59].First of all, the stimulation of light on the Au NPs surface causes a local surface charge density increase, leading to the emergence of a high localized electromagnetic field around the Au NPs, which penetrates into the phosphor. Finally, this strong electromagnetic field increases the luminescence emission by changing the crystal field around the activator ions. [49,60].

The absolute QY values measured are 10% and 5% for the Eu-doped molybdate with and without Au NPS, respectively, as summarized in Table 2, confirming that the Au NPs are truly favoring the Eu^{3+} emission. The absolute QY values are relatively low when compared to other Eu^{3+}-red classic phosphors as Y_2O_3:Eu^{3+} (19%) [61], but the values are comparable to other molybdate phosphors [62]. Also, to the best of our knowledge, this is the first time that the QY value is reported for the Eu^{3+}-doped $Y_2(MoO_4)_3$ phosphor.

The Ω_2 and Ω_4 Judd-Ofelt intensity parameters were calculated for the Eu-doped samples using the emission spectra shown in Fig. 8 and equations (3) and (4), and the data are summarized in Table 2. The Ω_2 parameter is correlated to Eu^{3+} site distortions due to changes in the Eu-O bond angles since the electric dipole $^5D_0 \rightarrow {}^7F_2$ transition is dependent on the Eu^{3+} local symmetry [62]. In this way, the relative

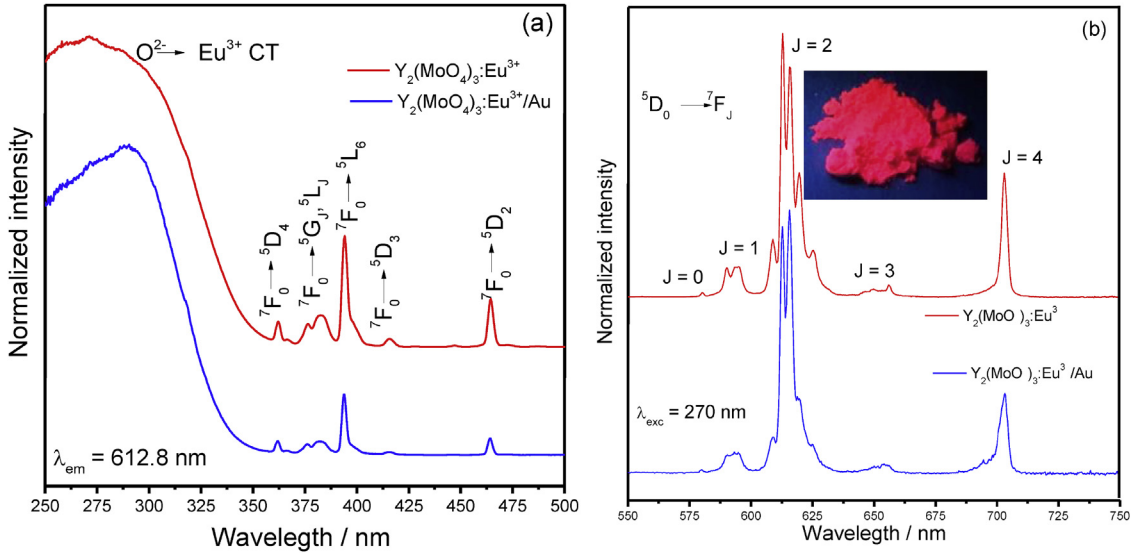

Fig. 8. Room-temperature excitation (a) and emission spectra (b) of the $Y_2(MoO_4)_3:Eu^{3+}$ particles prepared by Pechini's method. The insert in Figure (b) represents the $Y_2(MoO_4)_3:Eu^{3+}$/Au particles under 270 nm excitation.

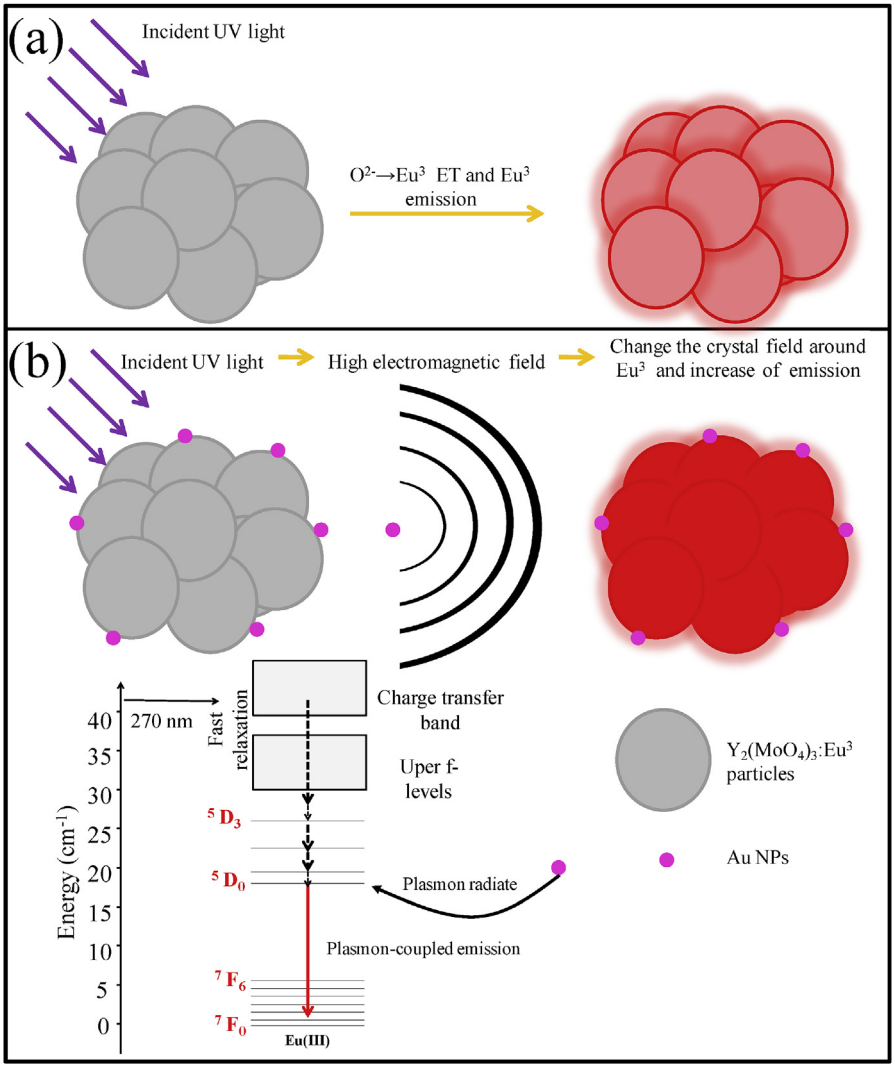

Fig. 9. Eu^{3+} emission Illustration of Eu^{3+} -doped $Y_2(MoO_4)_3$ without (a) and with (b) Au NPs.

Table 2
Experimental Judd-Ofelt intensity parameters (Ω_2, Ω_4), lifetime (τ) values obtained from a monoexponential fitting in the decay curves shown in Figure S5, radiative (A_{rad}) e nonradiative (A_{nrad}) rates obtained from the emission spectra and equations (3), (4) and (6), Eu^{3+} $^5D_0$ level quantum efficiency (η) obtained from equations (5)–(7), and emission quantum yield (QY) at 270 nm excitation for the Eu^{3+}-doped molybdates.

	Ω_2/pm^2	Ω_4/pm^2	τ/ms	A_{rad}/s^{-1}	A_{nrad}/s^{-1}	η/%	QY/%
$Y_2(MoO_4)_3$:Eu^{3+}	12.4	6.80	0.61	1444	195	88	5
$Y_2(MoO_4)_3$:Eu^{3+}/Au	15.3	8.4	0.53	1754	132	92	10

intensity of this hypersensitive transition increases with the decrease of Eu^{3+} local symmetry directly influencing the Ω_2 values [30]. Already the Ω_4 parameter is not directly influenced by the Eu^{3+} local symmetry, but indeed with the electron density of the ligands (L) around Eu^{3+}, which value decreases with the increase of the electron density of the ligand. Therefore, larger values of Ω_4 suggest a high covalence between Eu^{3+}-L bonds [63]. The relatively high Ω_2 values for the samples suggest that Eu^{3+} ions are inserted in low symmetry sites, and it is in agreement with the structural study since Eu^{3+} ions are replacing the Y^{3+} ions in octahedral-distorted YO_6 polyhedra. Furthermore, the water molecules present in the lattice cause distortions in molybdate structure, leading to distortions in the EuO_6 polyhedra. The gold nanoparticles are lowering the Eu^{3+} site symmetry since the Ω_2 increase when the system is incorporated with Au. This observation is in accordance with Raman measurements.

On the other hand, the low Ω_4 values suggest that the Eu-O bond are predominantly ionic yet there is a Ω_4 value increase when the Au NPs are inserted in the matrix, indicating an enhancement in the Eu-O bond covalence degree. In fact, L. Wang et al. [64] confirm the ionic nature of the Y-O bond and as the Eu^{3+} is replacing Y^{3+} ions in the molybdate lattice, it is reasonable to consider that the Eu-O bonds have predominant ionic nature.

The decay curves recorded monitoring the Eu^{3+} $^5D_0$ emitter level can be found in Figure S5, supplementary material, and both curves were best fitted using a monoexponential adjustment in order to determine the lifetime values. The lifetime values, in turn, were used to evaluate the Eu^{3+} $^5D_0$ quantum efficiency using equation (5), and (7), and the values are listed in Table 2. The prepared phosphors display quantum efficiency comparable to high-efficient red phosphors as $NaY(WO_4)_2$ (~90%) [65], YOF:Eu^{3+} (~96%) [66], and Y_2O_3:Eu^{3+} (~95%) [67], qualifying them to photonic applications. Also, the quantum efficiency increases to 92% when the Au NPs are present in the system due to the increase of the A_{rad} contribution, as previously shown.

4. Conclusion

In summary, high-crystalline Eu^{3+}-doped $Y_2(MoO_4)_3$ red phosphor incorporated with Au NPs were successfully synthesized by the Pechini's method. High-agglomerated and spheroidal-shaped molybdate particles with band gap of ~2.90 eV were obtained after the calcination step, and the Au NPs with a diameter of 46 nm are on the surface of these particles. The Eu^{3+} ions are forming a solid solution with the molybdate phase, replacing Y^{3+} ion, and occupying octahedral-distorted EuO_6 polyhedra. The Au incorporation is leading to distortion in the MoO_4 polyhedra, causing a symmetry lowering of the YO_6 and EuO_6 polyhedra. Moreover, water molecules in a proportion of $3H_2O$: $1Y_2(MoO_4)_3$ are leading to distortion in the molybdate lattice. The Eu^{3+}-doped molybdates emit light in the red region with 100% of color purity due to the radiative relaxation of the Eu^{3+} $^5D_0$ emitter level to the ^7F_J ground levels characteristic of Eu^{3+} in low symmetry sites. The Judd-Ofelt intensity parameters confirm that the Eu^{3+} ions are in low symmetry sites with Eu-O bonds predominantly ionic. The Au NPs enhance the Eu^{3+} radiative rate and quantum efficiency due to the excitation field enhancement caused by the local surface plasmon resonance absorption effect of Au NPs. Therefore, the high crystallinity, pure red emission under 270 nm excitation, and quantum efficiency of 92% make the $Y_2(MoO_4)_3$:Eu^{3+}/Au composite a potential candidate to photonic applications as a red-light converter.

Acknowledgements

The authors are thankful to the Brazilian agencies FAPESP, CNPq and CAPES for the financial research support. Airton Germano Bispo-Jr is particularly grateful to the São Paulo Research Foundation (FAPESP) for the award of some scholarships (Grant No.2012/13876-9, 2015/10394-1, and 2016/20421-9). Laboratório de Microscopia Eletrônica de Varredura (FCT-UNESP), High Resolution Microscopy Multiuser Laboratory (LabMic/UFG), research group in sol-gel (UNIFRAN), Laboratório de Filmes Nanoestruturados (FCT-UNESP), Laboratório Multiusuário de Análises Químicas (IQ/UNESP – Araraquara), and Laboratório de Materiais Cerâmicos (LaMaC, FCT-UNESP). LD Carlos from CICECO-Aveiro Institute of Materials (University of Aveiro) is acknowledged for the quantum yield measurements.

Appendix A. Supplementary data

Supplementary data related to this article can be found at http://dx.doi.org/10.1016/j.optmat.2018.06.023.

References

[1] X. Chen, J. Wang, C. Yang, Z. Ge, H. Yang, Fluorescence resonance energy transfer from $NaYF_4$:Yb,Er to nano gold and its application for glucose determination, Sens. Actuators B 255 (2018) 1316–1324.
[2] H. Park, J. Kim, M. Kim, Y. Cho, M. Kwon, Localized surface plasmon-enhanced emission from red phosphor with Au-SiO2 nanoparticles, Mater. Lett. 205 (2017) 145–149.
[3] S. Zhang, J. Wang, W. Xu, B. Chen, W. Yu, L. Xu, H. Song, Fluorescence resonance energy transfer between NaYF4:Yb,Tmupconversion nanoparticles and gold nanorods: near-infrared responsive biosensor for streptavidin, J. Lumin. 147 (2014) 278–283.
[4] H. Lin, L.J. Li, C.Y. Lei, X.H. Xu, Z. Nie, M.L. Guo, Y. Huang, S.Z. Yao, Immune-independent and label-free fluorescent assay for CystatinC detection based on protein-stabilized Au nanoclusters, Biosens. Bioelectron. 41 (2013) 256–261.
[5] L.Z. Hu, S. Han, S. Parveen, Y.L. Yuan, L. Zhang, G.B. Xu, Highly sensitive fluorescent detection of trypsin based on BSA-stabilized gold nanoclusters, Biosens. Bioelectron. 32 (2012) 297–299.
[6] Q. Han, L. Yan, C. Zhang, M. Zhang, T. Zhang, H. Zheng, Influence of Au nanoparticles on luminescence property of YF_3submicro structures doped with Yb^{3+} and Ho^{3+} (Eu^{3+}) ion, J. Alloy. Comp. 715 (2017) 322–328.
[7] S. Shankar, S. Abraham John, Sensitive and highly selective determination of vitamin B1 in the presence of other vitamin B complexes using functionalized gold nanoparticles as fluorophore, RSC Adv. 5 (2015) 49920–49925.
[8] F. Xie, Z. Dong, D. Wen, J. Yan, J. Shi, J. Shi, M. Wu, A novel pure red phosphor $Ca_8MgLu(PO_4)_7$:Eu^{3+} for near ultraviolet white light-emitting diodes, Ceram. Int. 41 (2015) 9610–9614.
[9] Z. Zhang, L. Liu, S. Song, J. Zhang, D. Wang, A novel red-emitting phosphor $Ca_9Bi(PO_4)_7$:Eu^{3+} for near ultraviolet white light-emitting diodes, Curr. Appl. Phys. 15 (2015) 248–252.
[10] A.G. Bispo Jr., S.A.M. Lima, A.M. Pires, Energy transfer between terbium and europium ions in barium orthosilicate phosphors obtained from sol-gel route, J. Lumin. 199 (2018) 372–378.
[11] K. Binnemans, Interpretation of europium(III) spectra, Coord. Chem. Rev. 295 (2015) 1–45.
[12] A.M. Pires, M.F. Santos, M.R. Davolos, E.B. Stucchi, T he effect of Eu ion doping concentration in Gd_2O_3 fine spherical particles, J. Alloy. Comp. 344 (2002) 276–279.
[13] A.G. Bispo Jr., D.A. Ceccato, S.A.M. Lima, A.M. Pires, Red phosphor based on Eu^{3+}-isoelectronically doped Ba_2SiO_4 obtained via sol–gel route for solid state lightning, RSC Adv. 7 (2017) 53752–53762.
[14] S. Wang, K.K. Rao, Y. Wang, Y. Hsu, S. Chen, Y. Lu, Structural characterization and

luminescent properties of a red phosphor series: Y_2-xEux(MoO4)$_3$ (x = 0.4–2.0), J. Am. Ceram. Soc. 92 (2009) 1732–1738.
[15] S. Laufer, S. Strobel, T. Schleid, J. Cybinska, A. Mudringc, I. Hartenbach, Yttrium (III) oxomolybdates(VI) as potential host materials for luminescence applications: an investigation of Eu^{3+}-doped $Y_2[MoO_4]_3$ and $Y_2[MoO_4]_2[Mo_2O_7]$, New J. Chem. 37 (2013) 1919–1926.
[16] Y. Tian, X. Qi, X. Wu, R. Hua, B. Chen, Luminescent properties of $Y_2(MoO_4)_3$:Eu^{3+} red phosphors with flowerlike shape prepared via coprecipitation method, J. Phys. Chem. C 113 (2009) 10767–10772.
[17] M. Aflaki, F. Davar, Synthesis, luminescence and photocatalyst properties of zirconitananosheets by modified Pechini method, J. Mol. Liq. 221 (2016) 1071–1079.
[18] M.R. Loghman-Estarki, R.S. Razavi, H. Edrisa, M. pourbafrany, H. Jamalb, R. Ghasemi, Life time of new SYSZ thermal barrier coatings produced by plasma spraying method under thermal shock test and high temperature treatment, Ceram. Int. 40 (2014) 1405–1414.
[19] E.C. Dreaden, A.M. Alkilany, X. Huang, C.J. Murphy, M.A. El- Sayed, The golden age: gold nanoparticles for biomedicine, Chem. Soc. Rev. 41 (2012) 2740–2779.
[20] K.S. Lee, M.A. El-sayed, Gold and silver nanoparticles in sensing and Imaging: sensitivity of plasmon response to size, shape, and metal composition, J. Phys. Chem. B 110 (2006) 19220–19225.
[21] R. Sardar, A.M. Funston, P. Mulvany, R.W. Murray, Gold nanoparticles: past, present, and future, Langmuir 25 (2009) 13840–13851.
[22] S. Schlücker, SERS microscopy: nanoparticle probes and biomedical applications, ChemPhysChem 10 (2009) 1344–1354.
[23] A.M. Pires, O.A. Serra, S. Haeer, H.U. Güdel, Low-temperature upconversion spectroscopy of nanosized Y_2O_3: Er, Yb phosphor, J. Appl. Phys. 98 (2005) 063529/1–0635297/7.
[24] A.M. Pires, O.A. Serra, M.R. Davolos, Morphological and luminescent studies on nanosizedEr, Yb–Yttrium oxide up-converter prepared from different precursors, J. Lumin. 113 (2005) 174–182.
[25] J.L. Ferrari, A.M. Pires, M.R. Davolos, The effect of Eu^{3+} concentration on the Y_2O_3 host lattice obtained from citrate precursors, Mater. Chem. Phys. 113 (2009) 587–590.
[26] S.D. Gates, C. Lind, Polymorphism in yttrium molybdate $Y_2Mo_3O_{12}$, J. Solid state chem, 180 (2007) 3510–3514.
[27] A.L. Patterson, TheScherrer formula for x-ray particle size determination, Phys. Rev. 56 (1939) 978–982.
[28] A.B. Murphy, Band-gap determination from diffuse reflectance measurements of semiconductor films, and application to photoelectrochemicalwater-splitting, Sol. Energy Mater. Sol. Cells 91 (2007) 1326–1337.
[29] P. Kubelka, F. Munk, EinBeitragzurOptik der Farbanstriche, Z. Tech. Phys. 15 (1931) 593–601.
[30] C. Kodaira, H.F. Britoa, O.L. Malta, O.A. Serra, Luminescence and energy transfer of the europium (III) tungstate obtained via the Pechini method, J. Lumin. 101 (2003) 11–21.
[31] A.P. Duarte, M. Gressier, M. Menu, J. Dexpert-Ghys, J.M.A. Caiut, S.J.L. Ribeiro, Structural and luminescence properties of silica-based hybrids containing new silylated-diketonatoeuropium(III) complex, J. Phys. Chem. C 116 (2012) 505–515.
[32] S.S. Batsanov, E.D. Ruchkin, I.A. Poroshina, Refractive Indices of Solids, Springer Briefs in applied Sciences and Technology, (2016).
[33] X. Bai, G. Caputo, Z. Hao, V.T. Freitas, J. Zhang, R.L. Longo, O.L. Malta, R.A.S. Ferreira, N. Pinna, Efficient and tuneablephotoluminescentboehmite hybrid nanoplates lacking metal activator centres for single-phase white LEDs, Nat. Commun. 5 (2014) 1–8.
[34] W. Lu, L. Cheng, J. Sun, H. Zhong, X. Li, Y. Tian, J. Wan, Y. Zheng, L. Huang, T. Yu, H. Yu, B. Chen, The concentration effect of upconversion luminescence properties in Er^{3+}/Yb^{3+}-codoped$Y_2(MoO_4)_3$ phosphors, Physica B 405 (2010) 3284.
[35] X. Liu, X. Ge, E. Liang, W. Zhang, Effects of Al particles and thin layer on thermal expansion and conductivity of Al–$Y_2Mo_3O_{12}$cermets, Chin. Phys. B 26 (2017) 118101–118105.
[36] B.A. Marinkovic, P.M. Jardim, F. Rizzo, R.R. de Avillez, Crystal structure and negative thermal expansion of metastable $Y_2Mo_3O_{12}$, Solid State Sci. 7 (2005) 1377–1383.
[37] B.P. Maheshwary, J. Singh, R.A. Singh, Singh, Luminescence properties of Eu^{3+}-activated $SrWO_4$nanophosphors-concentration and annealing effect, RSC Adv. 4 (2014) 32605–32621.
[38] S. Sumithra, A.M. Umarji, Hygroscopicity and bulk thermal expansion in $Y_2W_3O_{12}$, Mater. Res. Bull. 40 (2005) 167–176.
[39] S. Sumithra, A.M. Umarji, Role of crystal structure on the thermal expansion of $Ln_2W_3O_{12}$ (Ln = La, Nd, Dy, Y, Er and Yb), Solid State Sci. 6 (2004) 1313–1319.
[40] B.A. Marinkovic, P.M. Jardim, R.R. de Avillez, F. Rizzo, Negative thermal expansion in $Y_2Mo_3O_{12}$, Solid State Sci. 7 (2005) 1377–1383.
[41] M. Wu, L. Wang, Y. Jia, Z. Guo, Q. Sun, Theoretical study of hydration in $Y_2Mo_3O_{12}$: effects on structure and negative thermal expansion, AIP Adv. 5 (2015) 27126–27129.
[42] G. Busca, Differentiation of mono-oxo and polyoxo and of monomeric and polymeric vanadate, molybdate and tungstate species in metal oxide catalysts by IR and Raman spectroscopy, J. Raman Spectrosc. 33 (2002) 348–358.
[43] E.J. Liang, H.L. Huo, Z. Wang, M.J. Chao, J.P. Wang, Rapid synthesis of $A_2(MoO_4)_3$ (A = Y^{3+} and La^{3+}) with a CO_2 laser, Solid State Sci. 11 (2009) 139–143.
[44] T. Schleid, S. Strobel, P.K. Dorhout, P. Nockemann, K. Binnemans, I. Hartenbach, YF[MoO_4] and YCl[MoO_4]: two halide derivatives of yttrium ortho-Oxomolybdate: syntheses, structures, and luminescence properties, Inorg. Chem. 47 (2008) 3728–3735.
[45] R. Krishnan, J. Thirumalai, Up/down conversion luminescence properties of $(Na_{0.5}Gd_{0.5})MoO_4$:Ln^{3+} (Ln = Eu, Tb, Dy, Yb/Er, Yb/Tm, and Yb/Ho) microstructures: synthesis, morphology, structural and magnetic investigation, New J. Chem. 38 (2014) 3480–3491.
[46] S.F. Wang, K.K. Rao, Y.R. Wang, Y.F. Hsu, S.H. Chen, Y.C. Lu, Structural characterization and luminescent properties of a red phosphor series: Y_2-xEux(MoO4)$_3$ (x = 0.4-2.0), J. Am. Ceram. Soc. 92 (2009) 1732–1738.
[47] J. Su, G. Wang, Y. Li, R. Li, B. Xu, Y. Wang, J. Zhang, Synthesis, novel luminescence properties, and surface-enhanced Raman scattering of Au/Y_2O_3:Eu^{3+} composite nanotubes, Dalton Trans. 43 (2014) 14720–14725.
[48] A. Pandikumar, R. Ramaraj, Photocatalytic reduction of hexavalent chromium at gold nanoparticles modified titania nanotubes, Mater. Chem. Phys. 141 (2013) 629–635.
[49] Q. Han, L. Yan, C. Zhang, M. Zhang, T. Zhang, H. Zheng, Influence of Au nanoparticles on luminescence property of YF_3submicrostructures doped with Yb^{3+} and Ho^{3+} (Eu^{3+}) ions, J. Alloy. Comp. 715 (2017) 322–328.
[50] R. Velchuri, S. Palla, G. Ravi, N.K. Velduthi, J.R. Reddy, M. Vitha, Metathesis synthesis, characterization, spectral and photoactivity studies of $Ln_{2/3}MoO_4$ (Ln = La, Pr, Nd, Sm, Eu, Gd, Tb, Dy, Er and Y), J. Rare Earths 33 (2015) 837–845.
[51] A.P.A. Marques, D.M.A. Melo, C.A. Paskocimas, P.S. Pizani, M.R. Joya, E.R. Leite, E. Longo, Photoluminescent $BaMoO_4$ nanopowders prepared by complex polymerization method (CPM), J. Solid State Chem. 179 (2006) 671–678.
[52] J.H. Ryu, K.M. Kim, S.W. Mhin, G.S. Park, J.W. Eun, K.B. Shim, C.S. Lim, Laser-induced synthesis of $BaMoO_4$ nanocolloidal suspension and its optical properties, Appl. Phys. A 92 (2008) 407–412.
[53] P. Jena, S.K. Gupta, V. Natarajan, O. Padmaraj, N. Satyanarayana, M. Venkateswarlu, On the photo-luminescence properties of sol–gel derived undoped and Dy^{3+} ion doped nanocrystallineScheelite type $AMoO_4$ (A = Ca, Sr and Ba), Mater. Res. Bull. 64 (2015) 223–232.
[54] C. Cui, J. Bi, F. Shi, X. Lai, D. Gao, Unique photoluminescence properties of highly crystallized $BaMoO_4$ film prepared by chemical reaction, Mater. Lett. 61 (2007) 4525–4527.
[55] K. Nitsch, M. Nikl, M. Rodova, S. Santucci, Growth of lead tungstate single crystals from gel and their luminescence, Phys. Status Solidi 179 (1978) 261–264.
[56] Fu Wen, X. Zhao, H. Huo, J. Chen, E. Shu-Lin, J. Zhang, Hydrothermal synthesis and photoluminescent properties of $ZnWO_4$ and Eu^{3+}-doped $ZnWO_4$, Mater. Lett. 55 (2002) 152–157.
[57] W.T. Carnall, G.L. Goodman, K. Rajnak, R.S. Rana, A systematic analysis of the spectra of the lanthanides doped into single crystal LaF_3, J. Chem. Phys. 90 (1989) 3443–3457.
[58] Z. Chai, Z. Yang, A. Huang, C. Yu, J. Qiu, Z. Song, Preparation and photoluminescence enhancement of Au nanoparticles embedded LaPO4:Eu3+ inverse opals, J. Am. Ceram. Soc. (2018) 1–6.
[59] W. Ye, Q. Huang, X. Jiao, X. Liu, G. Hu, Plasmon-enhanced fluorescence of CaF_2:Eu^{2+}nanocrystals by Ag nanoparticles, J. Alloy. Comp. 719 (2017) 159–170.
[60] M.E. Koleva, N.N. Nedyalkov, P.A. Atanasov, J.W. Gerlach, D. Hirsch, A. Prager, B. Rauschenbach, N. Fukata, W. Jevasuwan, Porous plasmonicnanocomposites for SERS substrates fabricated by two-step laser method, J. Alloy. Comp. 665 (2016) 282–287.
[61] T. Hayakawa, M. Nogami, High luminescence quantum efficiency of Eu^{3+} - doped SnO_2–SiO_2 glasses due to excitation energy transfer from nano-sized SnO_2 crystals, Sci. Technol. Adv. Mater. 6 (2005) 66–70.
[62] [a] M. Janulevicius, J. Grigorjevaite, G. Merkininkaite, S. Sakirzanovas, A. Katelnikovas, Luminescence and luminescence quenching of $Eu_2Mo_4O_{15}$, J. Lumin. 179 (2016) 35–39;
[b] W.T. Carnall, Handbook on the Physics and Chemistry of Rare Earths, (1979).
[63] T. Grzyb, S. Lis, Structural and spectroscopic properties of LaOF: Eu^{3+}Nanocrystals prepared by the sol-gel Pechini method, Inorg. Chem. 50 (2011) 8112–8120.
[64] L. Wang, F. Wang, P. Yuan, Q. Sun, E. Liang, Y. Jia, Z. Guo, Negative thermal expansion correlated with polyhedral movements and distortions in orthorhombic $Y_2Mo_3O_{12}$, Mater. Res. Bull.48 (2013) 2724–2729.
[65] L. Ting, M. Qingyu, S. Wenjun, Luminescent properties of Eu^{3+} doped NaY$(WO_4)_2$nanophosphors prepared by molten salt method, J. Rare Earths 33 (2015) 915–921.
[66] T. Grzyb, M. Wecławiak, J. Rozowska, S. Lis, Structural and spectroscopic properties of YOF: Eu3+nanocrystals, J. Alloy. Comp. 576 (2013) 345–349.
[67] S. Som, S. Das, S. Dutta, H.G. Visser, M.K. Pandey, P. Kumar, R.K. Dubey, S.K. Sharma, Synthesis of strong red emitting Y_2O_3:Eu^{3+} phosphor by potential chemical routes: comparative investigations on the structural evolutions, photometric properties and Judd–Ofelt analysis, RSC Adv. 5 (2015) 70887–70898.